12th International Symposium on Turbulence and Shear Flow Phenomena (TSFP12)
Osaka, Japan, July 19–22, 2022

MECHANISMS OF INTERACTION BETWEEN A STATIONARY CROSSFLOW INSTABILITY AND BACKWARD-FACING STEPS

Oleksandr Krochak
Faculty of Aerospace Engineering
Delft University of Technology
Kluyverweg 1, 2629 HS Delft, the Netherlands
O.O.Krochak@student.tudelft.nl

Jordi Casacuberta
Faculty of Aerospace Engineering
Delft University of Technology
Kluyverweg 1, 2629 HS Delft, the Netherlands
J.CasacubertaPuig@tudelft.nl

Stefan Hickel
Faculty of Aerospace Engineering
Delft University of Technology
Kluyverweg 1, 2629 HS Delft, the Netherlands
S.Hickel@tudelft.nl

Marios Kotsonis
Faculty of Aerospace Engineering
Delft University of Technology
Kluyverweg 1, 2629 HS Delft, the Netherlands
M.Kotsonis@tudelft.nl

INTRODUCTION

Subsonic swept-wing aircraft is a main mode of long-distance passenger transport; thus, improving its efficiency carries a significant economic and environmental impact. Laminar Flow Control (LFC) technology has shown potential to reduce skin friction drag by delaying laminar-turbulent transition on the wings and tail parts. However, surface irregularities, such as two-dimensional steps, caused by panel junctions and joints, may alter the stability of the boundary layer, promote premature laminar-turbulent transition (Perraud & Seraudie, 2000), and reduce the effectivity of LFC. Stationary crossflow instabilities may typically dominate the transition path in swept-wing flows. The goal of this article is to investigate the purely stationary interaction between an imposed stationary crossflow instability developing in a swept-wing boundary layer and backward-facing steps of several heights.

Tufts *et al.* (2017) performed numerical simulations of backward-facing-step flows and reported rather mild stationary crossflow growth at the step, which they do not consider as the main mechanism promoting transition. Eppink (2022) studied the evolution of the crossflow instability over a backward-facing step via Particle Image Velocimetry (PIV) measurements. It is hypothesized that, as a consequence of the reversal of the crossflow velocity profile downstream of the step, stationary crossflow vortices rotating in a sense opposite to the original primary ones may be amplified. Casacuberta *et al.* (2021) carried out Direct Numerical Simulations (DNS) to study the stationary interaction between incoming crossflow and forward-facing steps. They observed that a system of near-wall streaky perturbation structures are induced at the step; these develop underneath the incoming crossflow perturbation locally around the step. The harmonic (i.e., smaller wavelength) components of the crossflow perturbation are significantly destabilized by the inflectional step-distorted base-flow profiles.

In this article, DNS are performed to study the purely stationary mechanisms of interaction between an incoming prescribed crossflow instability and backward-facing steps of various heights. The main elements of the setup of Casacuberta *et al.* (2021, 2022), namely the free-stream evolution, step heights and location, and stationary crossflow properties are reproduced in our present work to facilitate the direct comparison of mechanisms of interaction in backward- versus forward-facing steps. Reference data of a no-step case from their investigation is used for comparison. Unsteady perturbation effects ultimately leading the laminar-turbulent transition process are here discarded to isolate the stationary form of flow mechanisms; inclusion of unsteady structures in a possibly complex flow scenario would likely mask main mechanisms of the present analysis. The stationary perturbation field is decomposed in spanwise Fourier modes. The effect of step-induced base-flow features, such as recirculating flow, inflectional profiles, or local pressure gradient on altering the evolution of the stationary perturbation field is analyzed qualitatively and quantitatively.

METHODOLOGY

The incompressible swept-wing flow is modeled as flat-plate flow with an externally imposed airfoil-like pressure gradient in the chordwise direction. The free-stream velocity is decomposed into a chordwise component, u_∞, and a spanwise component, $w_\infty = -1.24u_\infty$, to model the effect of sweep angle. Pressure measurements from wind-tunnel experiments on a 45° swept wing (Rius-Vidales & Kotsonis, 2021) are used to guide the DNS setup. The inflow boundary layer thickness, $\delta_0 = 7.71 \times 10^{-4}$ m, and free-stream velocity, $u_\infty = 15.10$ m/s, are chosen as global characteristic quantities and used as non-dimensionalizing values. The reader is referred to Casacuberta *et al.* (2021, 2022) for further details on the flow problem and setup.

The main coordinate system reads $\mathbf{x} = [x\ y\ z]^T$, where x, y, and z indicate the chordwise (i.e. normal to the virtual leading edge), wall-normal and spanwise directions, respectively. A stationary crossflow mode, computed as solution to a local linear Orr-Sommerfeld analysis of the base flow profile, is prescribed at the inflow with an amplitude of $3.5 \times 10^{-3} u_\infty$ for all step cases. The DNS are performed for three different step heights, $h = \{0.59, 0.76, 0.97\}\delta_0$, all of which are below the undisturbed boundary layer thickness $\delta_{99,h}$ at the virtual lo-

cation of the step. Periodic boundary conditions are prescribed on the sides of the computational domain to constrain the perturbation growth in the chordwise direction. The spanwise domain length (i.e, the fundamental spanwise wavelength) is set to $\lambda_z = 7.5$ mm.

The DNS of the unperturbed two-dimensional spanwise-invariant base flow and the stationary developed three-dimensional flow are performed on an indentical computational domain. Letting $\mathbf{q} = [u\ v\ w\ p]^T$ be the vector of state variables, the steady developed flow, $\mathbf{q}(\mathbf{x})$, obtained from DNS is expressed as the sum of the spanwise-invariant laminar base flow, $\mathbf{q_b}(\mathbf{x})$, and a steady perturbation field, $\mathbf{q}'(\mathbf{x})$.

To gain insight on the perturbation behaviour, the field $\mathbf{q}'(\mathbf{x})$ is decomposed in spanwise Fourier modes:

$$q'_k = \sum_{j=0}^{N} A^k_{(0,j)} |\tilde{q}^k|_{(0,j)} \mathrm{e}^{\mathrm{i}(\phi^k_{(0,j)} + j\beta_0 z)}, \qquad (1)$$

where N is the number of modes considered, $k = \{u, v, w, p\}$ expresses a component of the state vector, $|\tilde{q}^k|_{(0,j)} = |\tilde{q}^k|_{(0,j)}(x,y)$ is the normalized shape function of a Fourier mode j, $A^k_{(0,j)} = A^k_{(0,j)}(x)$ is the amplitude, $\phi^k_{(0,j)}$ is the phase, $\mathrm{i} = \sqrt{-1}$, $\beta_0 = 2\pi/\lambda_z$ is the fundamental spanwise wavenumber, and λ_z is the fundamental spanwise wavelength, which is set equal to the spanwise domain length.

Following the discussion presented in Casacuberta *et al.* (2021), the base-flow components are decomposed based on the crossflow orientation. For that purpose, the local angle between the external inviscid streamline and the x-direction is evaluated. It reads $\phi(x) = \arctan(w_\infty/u_{\mathrm{ext}}(x))$, where u_{ext} denotes the external chordwise velocity in the outer-flow region. Accordingly, the base-flow velocity components *locally* tangent and orthogonal to the inviscid streamline direction are expressed as $u_{\mathrm{s,b}} = u_{\mathrm{b}}\cos(\phi) + w_{\mathrm{b}}\sin(\phi)$ and $w_{\mathrm{s,b}} = w_{\mathrm{b}}\cos(\phi) - u_{\mathrm{b}}\sin(\phi)$, where u_{b} and w_{b} are the base-flow chordwise and spanwise velocity components, respectively. The component $w_{\mathrm{s,b}}$ is the so-called crossflow velocity.

The incompressible Navier-Stokes equations are solved numerically with INCA, a conservative finite-volume solver (Hickel & Adams, 2008). The Navier-Stokes equations are marched in time with a third-order Runge-Kutta method. A fifth-order upwind scheme is used to discretize the convective terms. The Selective Frequency Damping (SFD) method (Åkervik *et al.*, 2006; Casacuberta *et al.*, 2018) is applied to numerically enforce a fully stationary solution of the developed flow. As convergence criterion, the L_2-norm of the SFD residual is chosen to be $\varepsilon = 10^{-6}$.

The computational domain encompasses $0 \le x/\delta_0 \le 517$, $y_{\mathrm{st}}/\delta_0 \le y/\delta_0 \le 26$ and $-4.86 \le z/\delta_0 \le 4.86$; the baseline flat plate is set at $y = 0$ and the step extends until $y_{\mathrm{st}}/\delta_0 = -0.59, -0.76, -0.97$ for step cases I, II, and III, respectively. For all cases, the step is located at $x/\delta_0 = 177.62$. The coordinate expressing the chordwise distance relative to the step is hereafter denoted by $x_{\mathrm{st}} = x - 177.62\delta_0$ and, downstream of the step, the relative wall-normal distance is denoted by $y^* = y - y_{\mathrm{st}}$. The results presented in this article have been obtained with a grid containing 2×10^6 and 3.7×10^7 cells for the base- and developed-flow runs, respectively. The reader is referred to Casacuberta *et al.* (2022) for further details on the topology of the computational grid.

Table 1: Base-flow properties in the near-step region.

Case	Step I	Step II	Step III
h/δ_0	0.59	0.76	0.97
$h/\delta_{99,h}$	0.31	0.40	0.52
$l_{\mathrm{rev}}/\delta_0$	9.6	12.8	17.2
$l_{\nabla p}/\delta_0$	13.3	17.1	20.5
$l_{w_{\mathrm{s,b}}}/\delta_0$	26.7	31.9	38.3
$\lvert u_{\mathrm{rev}}\rvert$ (%)	5.6	6.8	8.25
$\lvert w^{\mathrm{rev}}_{\mathrm{s,b}}\rvert$ (%)	10.0	12.0	14.5

RESULTS AND DISCUSSION

1 BASE-FLOW FEATURES

The presence of the step distorts the organization of the boundary-layer flow and introduces new base-flow structures which are not present in the reference, i.e., no-step, case. The most prominent feature of the base flow is recirculating flow immediately downstream of the step, see Figure 1(*a*). Its geometrical properties are here characterized by an isoline of $u_{\mathrm{b}} = 0$; see Table 1. The $x_{\mathrm{st}} = l_{\mathrm{rev}}$ denotes the stagnation point further downstream. The strength of the recirculating flow, i.e., the maximum reverse velocity, $|u_{\mathrm{rev}}|$ with $u_{\mathrm{rev}} < 0$, attains between 6% and 8% relative to u_{ext} in the step cases (Table 1). Such values are close to the threshold for a global instability to develop in classic pressure-driven separation bubbles (Rodríguez *et al.*, 2013). However, by constraining the interaction to be stationary via the usage of SFD, no manifestation of a possible global instability was captured.

The pressure field is locally altered by the presence of the step. A region of strong adverse pressure gradient arises immediately downstream of the step. It extends up to approximately $x_{\mathrm{st}}/\delta_0 = 20.5$ in step case III (Table 1); here, $l_{\nabla p}$ denotes the distance from $x_{\mathrm{st}} = 0$ to the threshold $\partial p/\partial x = 0$ downstream of the step at the wall. Furthermore, a region of enhanced favourable pressure gradient develops immediately upstream of the step. The pressure field around the step in the present DNS is in qualitative agreement with that reported by Tufts *et al.* (2017).

Casacuberta *et al.* (2022) report a strong modulation of the base-flow streamlines in z locally around the corner of a forward-facing step for a setup identical to the one presented here. In the current backward-facing-step flow, no significant deflection of the streamlines in z upstream of the step is observed. This may be ascribed to the different pressure-gradient strength induced upstream of the forward- versus the backward-facing step. In fact, the overall organization of the flow upstream of the step appears to not be significantly altered by the presence of the backward-facing step. Downstream of the step, the evolution of the flow in x above the flow-separation region is rather *gradual*. Contrary to the forward-facing step case (Casacuberta *et al.*, 2022), the streamlines of the flow do not visually display an abrupt turn in the x-z plane.

Next to flow reversal (i.e., $u_{\mathrm{b}} < 0$), the step induces reversal of the crossflow profile (i.e., $w_{\mathrm{s,b}} < 0$) as well; see Figure 1(*b-g*). The peak magnitude of the reserved crossflow profile in y, denoted by $|w^{\mathrm{rev}}_{\mathrm{s,b}}|$, is 10% and 15% relative to u_{ext} in

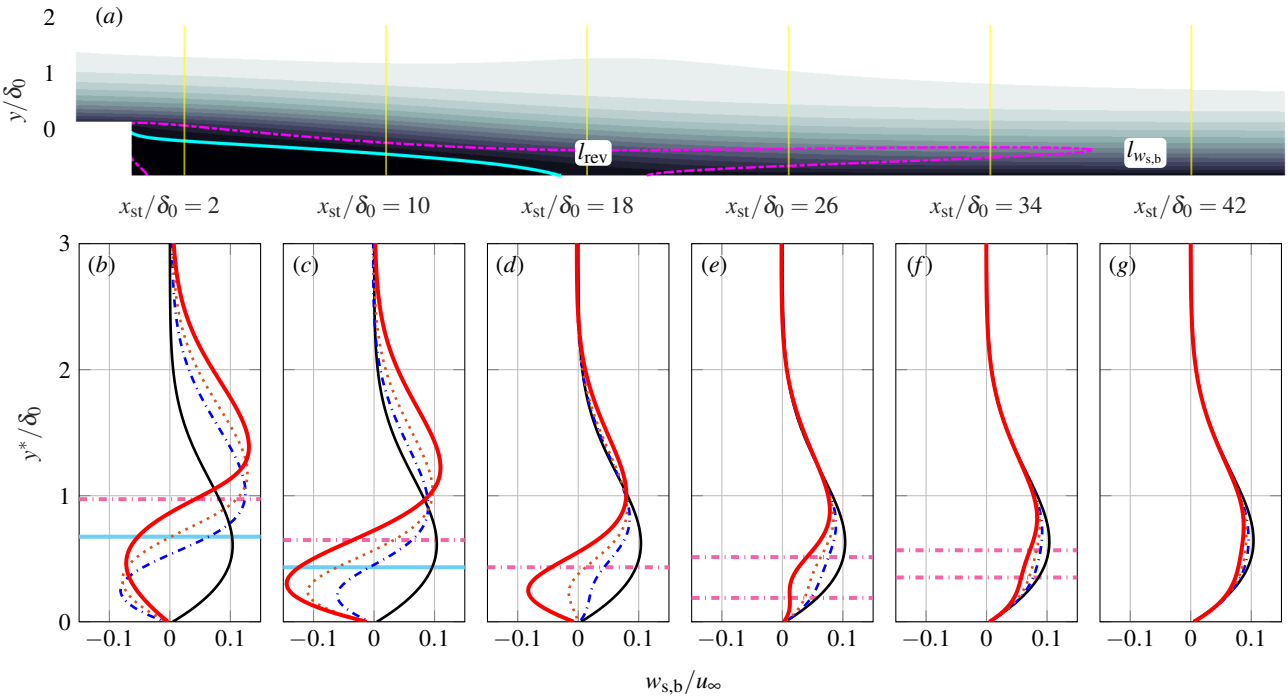

Figure 1: Contour of base-flow velocity, u_{b}, in step III (a). Evolution in x of the crossflow profile, $w_{\mathrm{s,b}}$, for the reference no-step (thin solid black), step I (dash-dotted blue), step II (dotted orange), and step III (thick solid red) cases (b-g). Isolines of velocity reversal $u_{\mathrm{b}} = 0$ (solid cyan) and crossflow inflection points $\partial^2 w_{\mathrm{s,b}}/\partial y^2 = 0$ (dash-dotted magenta).

step cases I and III, respectively (Table 1). It is noteworthy to mention that the evolution of the crossflow profile in x is in close qualitative agreement with the behaviour reported by Eppink (2022): surprisingly, close downstream of the step, the strength of the crossflow reversal is approximately similar for all steps studied here. However, when moving further in x, the reversed-flow strength is the greatest for the largest step case (Figure 1(c,d)).

The crossflow-reversal region downstream of the step is accompanied by additional inflection points in the crossflow profile that do not manifest in the reference case. These new inflection points arise close to the wall, underneath the original (primary) crossflow inflection points. The length in x of this region featuring secondary step-induced inflection points, $l_{w_{\mathrm{s,b}}}$, increases with the step height; see Table 1.

2 FUNDAMENTAL PERTURBATION EVOLUTION

Next, the behaviour of the fundamental perturbation component, i.e., the primary perturbation Fourier mode $\beta = \beta_0$, is analyzed. The discussion is restricted to near-step effects. Figure 2(a) portrays the chordwise evolution of the amplitude of the primary Fourier mode. Upstream of the step, the amplitude curves of the step cases are essentially identical to that of the no-step reference case. This was expected since, as it was previously mentioned, the steps have only a very weak upstream influence. Close downstream of the step, the fundamental perturbation component is significantly stabilized. This local stabilizing effect appears to be proportional to the step height (Figure 2(a)). Similarly, Casacuberta *et al.* (2022) report a local stabilizing influence of sufficiently large forward-facing steps to the incoming fundamental stationary crossflow perturbation.

When considering the evolution of the overall amplitude function, $A^{\tilde{u}}_{(0,1)}|\tilde{q}^u|_{(0,1)}$, a prominent additional peak develops in step cases II and III for $x_{\mathrm{st}} > 0$ close to the wall (Figure 3(a)). This topological feature has been reported for forward-facing (Tufts *et al.*, 2017; Casacuberta *et al.*, 2022), as well as for backward-facing-step flows (Eppink, 2022). In step case I this near-wall peak in the perturbation shape is either not present or very weak; see Figure 3(c). In step case III, the location of the additional peak in y reasonably matches the spatial location of the step-induced inflection points in the base flow.

The amplitude of the near-wall peak in step case III grows rapidly in x and, eventually, slightly surpasses the strength of the primary upper peak; see Figure 3(a). The primary peak of the perturbation shape may be associated to the original crossflow perturbation that develops further off the wall. In recent forward-facing-step flow investigations, the secondary near-wall peak downstream of the step was associated to the manifestation of spanwise-alternating perturbation streaks induced at the step corner (Casacuberta *et al.*, 2021, 2022). Despite topological similarities between such additional peaks in forward- versus backward-facing-step flows, in the present case, the near-wall peak in the perturbation shape may be representing a different flow mechanism than the one reported for forward-facing steps.

Eppink (2022) proposes that the destabilizing influence of new step-induced inflection points downstream of the step triggers stationary-crossflow growth. In the present DNS, the appearance of the secondary perturbation peak near the wall within the x-region featuring reversed crossflow seems to support the observations of Eppink (2022). In particular, visual correlation is found between the step-induced inflection point location and the perturbation amplification near the wall (Figure 3(a)).

To shed light on the nature of the mechanism feeding perturbation growth, the perturbation shape functions and growth rates from DNS are next compared to the results of linear sta-

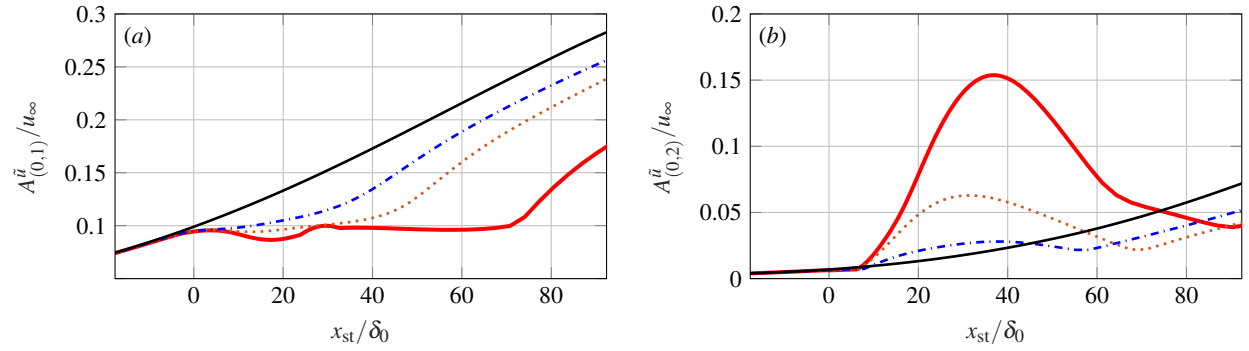

Figure 2: Evolution of the amplitude of the chordwise-velocity perturbation Fourier modes $\beta = \beta_0$ (*a*) and $\beta = 2\beta_0$ (*b*). Reference no-step (thin solid black), step I (dash-dotted blue), step II (dotted orange), and step III (thick solid red).

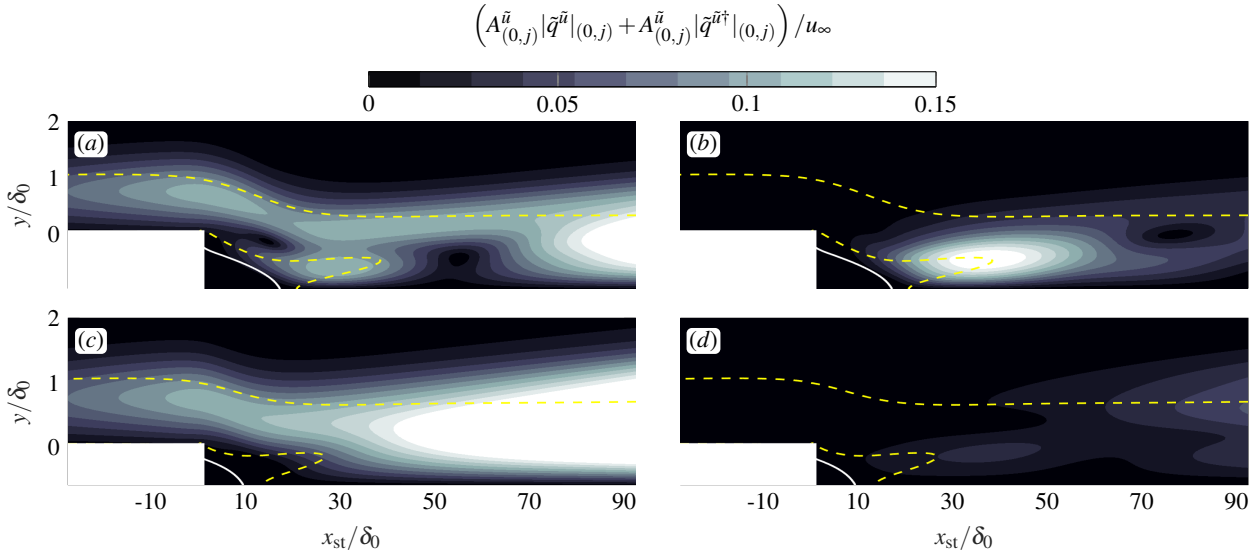

Figure 3: Chordwise-velocity perturbation amplitude function in step cases III (*a*,*b*) and I (*c*,*d*) for $\beta = \beta_0$ (*a*,*c*) and $\beta = 2\beta_0$ (*b*,*d*) Fourier modes. Base-flow reversal $u_b = 0$ (solid white), base-flow crossflow inflection points $\partial^2 w_{s,b}/\partial y^2 = 0$ (dashed yellow).

bility analysis. A linear local Orr-Sommerfeld (OS) eigenvalue problem is solved on the DNS base flow for the reference and step cases from the downstream vicinity of the step until approximately $x_{st}/\delta_0 = 82$. The analysis is carried out for $\beta = \beta_0$ to characterize fundamental perturbation effects. While the flow field is highly non-parallel close to the step, the results of an OS analysis are expected to elucidate on possible (in)stability effects associated to the inflectional base-flow profiles.

Downstream of all steps, two main unstable OS eigensolutions are identified. One is associated to the original crossflow mode and, as such, it is also captured in the reference case; this is mainly supported by the close match between the DNS perturbation shape and the eigenfunction associated to this eigenmode (see solid red line and blue circles in Figure 4(*e*), respectively). In addition, a new unstable OS eigensolution is identified in all step cases, which is not present in the reference case.

The trajectory in the complex plane of the aforementioned two families of OS eigenvalues as a function of x is depicted in Figure 4(*a-d*) for all cases studied. Here, $\alpha^{OS} = \alpha_r^{OS} + i\alpha_i^{OS}$ denotes the corresponding eigenvalues. As mentioned previously, shortly downstream of the step, the incoming crossflow mode is stabilized for all step cases in the DNS (Figure 2(*a*)). Conformably, the eigenvalue associated to the OS crossflow mode initially lies in (or close to) the stable region of the eigenspectrum. When moving in x, it gradually shifts towards the unstable half-plane. This is consistent with the DNS results; see Figure 2(*a*). Sufficiently downstream of the step in all step cases, the properties of the OS eigenmode originally associated to the crossflow mode gradually resemble those displayed by the reference case. Next to growth rate, the peak location in y of the OS eigenfunction associated to the crossflow mode reasonably matches that of the DNS shape function sufficiently downstream of the step; see Figure 4(*f*).

Considering the outcome of the analysis to this point, it can be hypothesized that the second family of unstable OS eigenmodes only identified in the step cases is associated to an inflectional instability supported by the step-distorted base-flow profiles. The fact that the wall-normal peak of the OS eigenfunction approximately coincides with the y-location of the step-induced inflection point in the base flow (Figure 4(*e*) and Figure 1(*c*)) would further strengthen this claim. The growth rates of this second family of eigenmodes largely exceeds that of the original crossflow; see Figure 4(*b-d*). This may highlight the strongly unstable nature of this new instability mechanism and would serve as a plausible explanation for the large perturbation amplification captured in the DNS

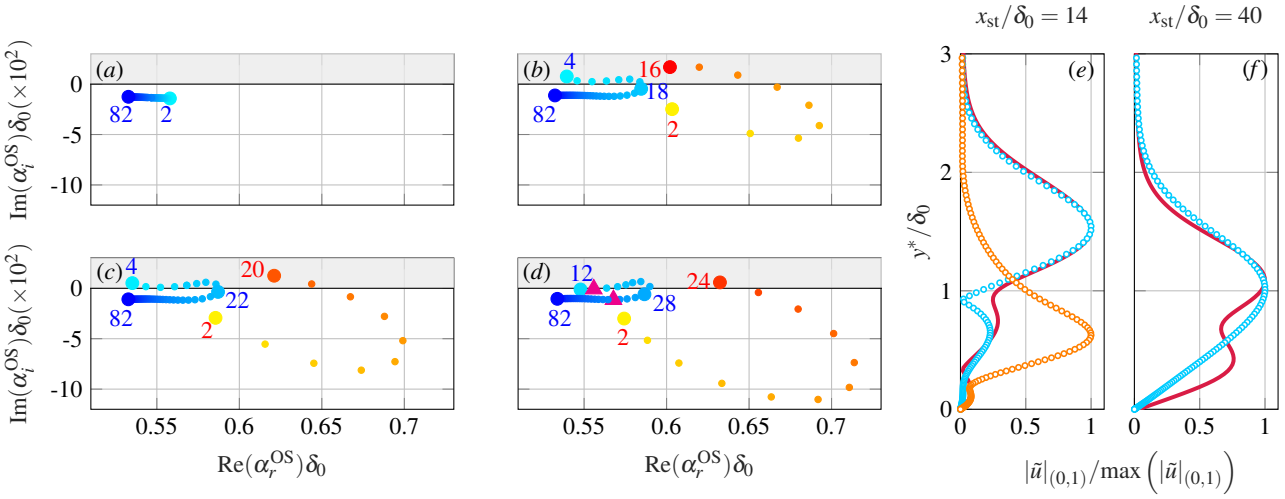

Figure 4: Trajectory of Orr-Sommerfeld eigenvalues in the range $x_{st}/\delta_0 \in [2, 82]$ (bright-to-dark for increasing x) for the reference no-step (*a*), step I (*b*), step II (*c*), and step III (*d*) cases. Numerals indicate x_{st}/δ_0 locations. Orr-Sommerfeld shape functions for $\beta = \beta_0$ (orange and blue circles) and DNS (solid red) at $x_{st}/\delta_0 = 14$ (*e*) and 40 (*f*) for step III indicated by magenta triangles in (*d*).

close to the wall in step case III; see Figure 3(*a*). Naturally, as the step height is decreased, the destabilizing influence of the inflection points weakens. This is consistently observed both in the DNS amplitude evolution (Figure 3(*a,c*)) and in the OS eigenspectrum (Figure 4(*b-d*)). Furthermore, it should be noted that this family of new eigenmodes in the step cases only manifests approximately in the chordwise region where the additional step-induced inflection points develop.

3 HARMONIC PERTURBATION EVOLUTION

The analysis is next extended to the harmonic (i.e., smaller wavelength) perturbation behaviour. For perturbations with $\beta = 2\beta_0$, amplification is measured downstream of x_{st} in all step cases (Figure 2(*b*)). Significant amplification is observed for the harmonics $\beta = 3\beta_0$, $\beta = 4\beta_0$, and $\beta = 5\beta_0$ as well, see Figure 5. For the sake of simplicity, the discussion is here focused on the $\beta = 2\beta_0$ mode since it is representative of the main qualitative harmonic behaviour. For the largest step case, the amplitude of the Fourier mode $\beta = 2\beta_0$, $A^{\tilde{u}}_{(0,2)}$, surprisingly exceeds that of the fundamental mode, $\beta = \beta_0$, immediately downstream of the step (Figure 2). The main peak of the shape function $|\tilde{q}^u|_{(0,2)}$ in y arises close to the location of the secondary near-wall peak in the profile of the fundamental Fourier mode (Figure 3(*a,b*)). This feature is observed in all step cases. Following the discussion provided in the previous section, the present results suggest a destabilizing influence of the step-induced inflection point to perturbation with $\beta = 2\beta_0$ as well.

In a fashion similar to the analysis of the fundamental perturbation component, $\beta = \beta_0$, an Orr-Sommerfeld eigenvalue problem is here solved for $\beta = 2\beta_0$. An unstable eigensolution is identified, which does not manifest in the reference no-step case. Figure 6(*a-d*) depicts the evolution of the associated eigenvalue in the complex plane as a function of x, and Figure 6(*e*) portrays the corresponding OS eigenfunction together with the DNS profile. Initially in x, the OS eigenvalue lies in the unstable region implying that, in agreement with the DNS results, the base flow is destabilizing. This is not the case in the reference no-step configuration since the harmonic growth is mainly driven by non-linear perturbation interactions. Correspondingly, the associated OS eigenvalue remains in the stable region for all x. Interestingly, the trajectory in the complex plane of this new unstable eigenvalue manifesting in the step cases for $\beta = 2\beta_0$ (Figure 6(*b-d*)) closely follows that of the additional unstable eigenvalue in the $\beta = \beta_0$ space. The peak in y of the associated $\beta = 2\beta_0$ OS eigenfunction at $x_{st}/\delta_0 = 10$ matches the y-location of the peak from DNS and lies close to the step-induced inflection point (Figure 6(*e*) and Figure 1(*c*)). Therefore, the present results provide evidence that the harmonic field is significantly destabilized at the step due to an inflectional instability associated to the base-flow distortion introduced by the step.

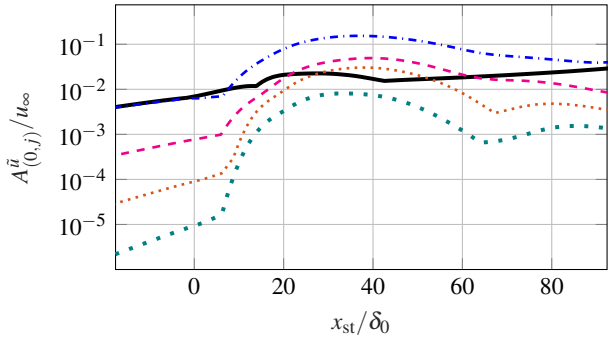

Figure 5: Evolution of the amplitude of the chordwise-velocity perturbation Fourier modes $\beta = 0$ (thick solid black), $\beta = 2\beta_0$ (dash-dotted blue), $\beta = 3\beta_0$ (dashed magenta), $\beta = 4\beta_0$ (dotted orange), $\beta = 5\beta_0$ (loosely dotted teal) for step III.

CONCLUSIONS

Direct Numerical Simulations (DNS) are performed to study the interaction between an imposed stationary crossflow mode and backward-facing steps of several heights immersed in an incompressible three-dimensional swept-wing boundary layer. The behaviour of the unperturbed laminar base flow and the stationary perturbation field at the step are presented and

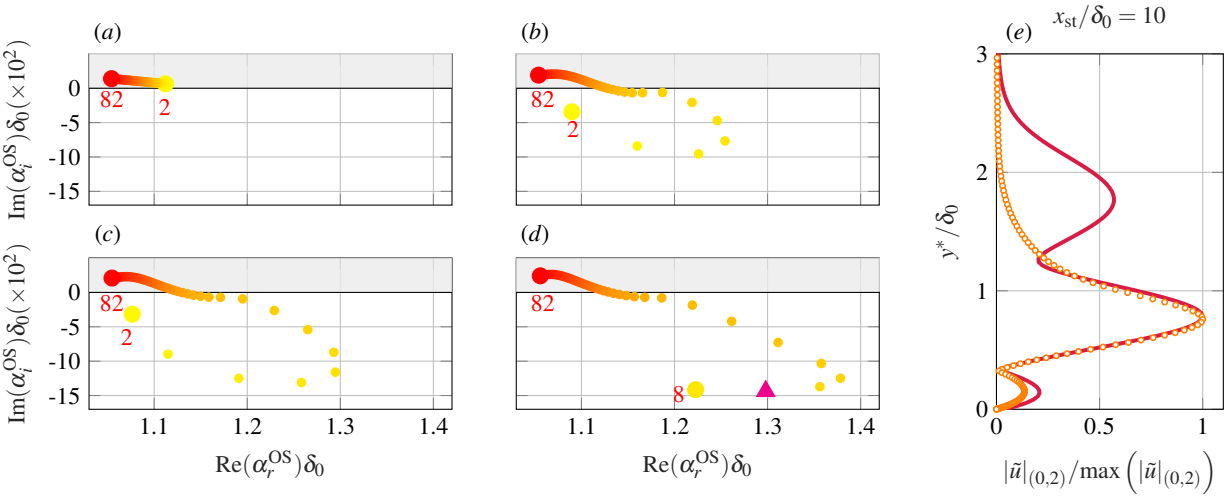

Figure 6: Trajectory of Orr-Sommerfeld eigenvalues for the reference no-step case (*a*), step I (*b*), step II (*c*), and step III (*d*) for $\beta = 2\beta_0$. Orr-Sommerfeld shape function (orange circles) and DNS (solid red) for step III at $x_{st}/\delta_0 = 10$ (*e*) indicated by a magenta triangle in (*d*).

discussed. The analysis is restricted to the near-step regime and to perturbation effects of stationary nature. To illustrate similarities and differences with main mechanisms and structures in forward-facing-step flows, the present setup is identical to that employed in recent numerical investigation on forward-facing steps (Casacuberta *et al.*, 2021, 2022).

Both the chordwise extension and peak reverse velocity of the flow-separation region downstream of the backward-facing steps are significantly larger than in forward-facing steps of identical height. The base-flow profiles downstream of the backward-facing step display two families of inflection points in the crossflow component; one is associated to the original inflection point also present in the reference no-step case. The second is induced by the presence of the step.

It is found that locally around the step, the fundamental crossflow perturbation is stabilized. At the same time, perturbation amplification is measured close to the near-wall inflection point location, suggesting a destabilizing influence of the latter. The DNS results are compared to the results of a linear local Orr-Sommerfeld (OS) stability analysis on the DNS base flow. For perturbations associated to the fundamental spanwise wavelength, two main unstable eigensolutions are identified and associated to 1) the original stationary crossflow mode and 2) an inflectional instability that would be associated to a new family of near-wall inflection points induced by the step.

When considering the harmonic perturbation field of smaller wavelength, a significant destabilization is measured close to the step. An OS unstable eigenmode is identified for perturbations with half the fundamental wavelength; the topology of the associated OS eigenfunction and the results of the overall analysis suggest that the step-induced near-wall inflectional profiles support an inflectional instability for harmonic wavelengths as well. Similar as in forward-facing-step flows, the inflectional profiles induced by the step support significant destabilization of the harmonic perturbation components.

The underlying inflectional instability is proposed as a main step-flow mechanism purely driven by the base flow modification imparted by the step. Furthermore, based on the aforementioned considerations, we conclude that the results of the OS analysis provide insightful information on the nature and evolution of the stationary perturbation field.

REFERENCES

Åkervik, E., Brandt, L., Henningson, D. S., Hœpffner, J., Marxen, O. & Schlatter, P. 2006 Steady solutions of the Navier-Stokes equations by selective frequency damping. *Phys. Fluids* **18** (6), 068102.

Casacuberta, J., Groot, K. J., Tol, H. J. & Hickel, S. 2018 Effectivity and efficiency of selective frequency damping for the computation of unstable steady-state solutions. *J. Comp. Phys.* **375**, 481–497.

Casacuberta, J., Hickel, S. & Kotsonis, M. 2021 Mechanisms of interaction between stationary crossflow instabilities and forward-facing steps. In *AIAA Scitech 2021 Forum*, p. 0854.

Casacuberta, J., Hickel, S., Westerbeek, S. & Kotsonis, M. 2022 Direct Numerical Simulation of interaction between a stationary crossflow instability and forward-facing steps. *J. Fluid Mech. [under consideration for publication]* .

Eppink, Jenna L 2022 Mechanisms of instability growth, interaction and breakdown induced by a backward-facing step in a swept-wing flow. *J. Fluid Mech.* **931**.

Hickel, S. & Adams, N.A. 2008 Implicit LES applied to zero-pressure-gradient and adverse-pressure-gradient boundary-layer turbulence. *Int. J. Heat and Fluid Flow* **29** (3), 626–639.

Perraud, J. & Seraudie, A. 2000 Effects of steps and gaps on 2D and 3D transition. *ECCOMAS* pp. 11–14.

Rius-Vidales, A. & Kotsonis, M. 2021 Impact of a forward-facing step on the development of crossflow instability. *J. Fluid Mech.* **924**, A34.

Rodríguez, D., Gennaro, E. & Juniper, M. 2013 The two classes of primary modal instability in laminar separation bubbles. *J. Fluid Mech.* **734**, R4.

Tufts, M., Reed, H., Crawford, B., Jr, G. Duncan & Saric, W. 2017 Computational investigation of step excrescence sensitivity in a swept-wing boundary layer. *J. Aircraft* **54** (2), 603.